

Fluorescence lifetime microscopy with a time- and space-resolved single-photon counting detector

X. Michalet^{1a}, O.H.W. Siegmund^b, J.V. Vallerga^b, P. Jelinsky^b,
F. F. Pinaud^a, J.E. Millaud^c, S. Weiss^a

^a Department of Chemistry & Biochemistry, University of California at Los Angeles
607 Charles E. Young Drive E., Los Angeles, CA 90095, USA

^b Experimental Astrophysics Group, Space Sciences Laboratory
University of California at Berkeley, 7 Gauss Way, Berkeley, CA 94720, USA

^c Advanced Detector Group, Lawrence Livermore National Laboratory
7000 East Avenue, Livermore, CA 94550, USA

ABSTRACT

We have recently developed a wide-field photon-counting detector (the H33D detector) having high-temporal and high-spatial resolutions and capable of recording up to 500,000 photons per sec. Its temporal performance has been previously characterized using solutions of fluorescent materials with different lifetimes, and its spatial resolution using sub-diffraction objects (beads and quantum dots). Here we show its application to fluorescence lifetime imaging of live cells and compare its performance to a scanning confocal TCSPC approach. With the expected improvements in photocathode sensitivity and increase in detector throughput, this technology appears as a promising alternative to the current lifetime imaging solutions.

Keywords: single-photon, single-molecule, photocathode, microchannel plate, position sensitive anode, fluorescence, lifetime, FLIM, quantum dot, live cell

1. INTRODUCTION

A powerful extension of fluorescence microscopy, fluorescence lifetime microscopy measures the fluorescence temporal decay properties of excited fluorophores at different locations in a sample (for recent reviews see ref. ¹⁻⁴). Two main strategies exist to acquire this information: time-domain or frequency-domain data acquisition. In the time-domain approach, which is the only one which will be discussed here, pulsed laser excitation is used and the probability distribution of fluorescence emission as a function of the delay after excitation is measured. Different mathematical treatments can then be used to extract single or multiple fluorescence lifetimes and their respective contribution to the emitted signal. This information is used to infer the relative abundance of fluorescence emitters or the nature of their environment. In particular, this approach can be used to map the level of fluorescence resonance energy transfer (FRET) between a donor and an acceptor fluorophores, which reports on their respective distance ⁵. For instance, when the fluorophores are attached to two different types of proteins, this map gives information on the distance between these proteins, therefore allowing the study of protein-protein interaction.

Many time-domain techniques have been developed, which can be differentiated by the geometric configurations of the excitation and emission paths and the type of detector used to collect the fluorescence, among other characteristics. The most commonly used time-domain techniques are (i) scanning confocal microscopy using time-correlated single-photon counting (TCSPC) detection and (ii) wide-field microscopy using time-gated camera detection. For the sake of completeness, we mention here the less common line-scanning techniques based on streak cameras ⁶.

Scanning confocal lifetime microscopy forms an image of the sample by exciting it locally (within a diffraction-limited volume) and collecting the fluorescence light emitted from within this small volume. The excitation spot is then raster-scanned in two dimensions to form an image comprised of as many pixels as there were excitation locations.

Two distinct strategies can be adopted to achieve fluorescence excitation and detection at a localized point. In the most commonly implemented, one-photon excitation (1-PE) of the fluorescence is achieved using a moderate intensity laser line (a few μW of laser power are injected into the sample). The resulting excitation takes place mostly at the focal point of the objective lens use to observe the sample, but some residual excitation also occurs along the light path throughout

¹ michalet@chem.ucla.edu; Ph: 1 310 794-6693 ; Fax: 1 310 267-4672

the sample, leading to significant out-of-focus fluorescence contamination. This contamination is efficiently eliminated by a pinhole placed at the focal plane of the tube lens of the microscope, or a conjugate plane in the detection path. The other implementation uses two-photon excitation (2-PE) of the fluorescence. In this process, photons of typically twice the wavelength used in 1-PE are employed, necessitating the use of different lasers. Also, due to the very small 2-PE absorption cross-section of most fluorophores, much higher laser power are needed (several mW are generally injected into the sample). The advantages of this approach however, is that the excitation probability being proportional to the square of the local incoming laser intensity, the region where a significant level of fluorescence emission occurs is much more limited than in the 1-PE case, obviating the use of pinhole in the detection path. An exhaustive discussion of the merits and limitations of both implementations is beyond the scope of this introduction, but it was important to remind their existence, since such a choice does not exist in the wide-field geometry⁷. In both implementations, the image obtained corresponds to an optical slice of the sample perpendicular to the optical axis, allowing forming a 3-dimensional representation of the sample by acquiring several slices at different focal depths. As we will discuss next, this is much more difficult to achieve (if at all) in a wide-field configuration. For both 1-PE and 2-PE, the signal level per pixel is proportional to the product of the local excitation rate and the integration time. The total duration of the acquisition is proportional to the number of pixels in the image. Typical detectors used in TCSPC are single-photon avalanche photodiodes (SPAD) or photomultipliers (PMT) outputting a brief voltage pulse for each detected photon⁸. The time interval between these individual pulses and the next laser pulse are measured by fast dedicated electronics, and further processed to form fluorescence decay histograms². In order to perform this type of measurement, at most one photon needs to be detected at a time. Since these detectors (and the associated electronics) have a dead-time of several dozens of nanoseconds (ns), a maximum count rate of a few MHz is possible. In practice, experiments use detected count rates much less than 1 MHz.

In the wide-field configuration, the sample is excited over a large area by a defocused (pulsed) laser beam, and the emitted fluorescence collected onto a wide-field detector. To obtain temporal information, intensified detectors which can be time-gated have been used almost exclusively until recently. In this configuration, the detector accumulates the signal over a finite integration time (instead of detecting individual photons), but during this integration time (say, 1 s), only photons emitted during a short (sub-ns) time window after each excitation pulse are actually detected. This is obtained by turning the intensifier stage of the camera on and off very rapidly after each laser pulse (billions of pulses are generated during the integration time, allowing for a sufficient signal to be accumulated). By accumulating several images obtained at different delays of the time gate with respect to the laser pulse, a coarse fluorescence decay histogram can be built for each pixel location.

There are marked differences between both approaches. The scanning TCSPC methods allow potentially very detailed fluorescence decays to be obtained, since the timing electronics can usually measure the arrival time of each photon with more than 10 bits of resolution (dynamic range: 1,024). It also provides highly contrasted images, due to the absence of out-of-focus fluorescence contamination. However, it requires forming the image pixel by pixel. The wide-field time-gated approach acquires information on all pixels in parallel, but on the other hand, the resolution of the fluorescence decay histogram is limited to the number of time gates N (dynamic range: $N \ll 1,024$). Also, the acquisition is very photon-inefficient, as photons arriving outside of the current time-gate are not detected, and out-of-focus fluorescence significantly reduces the image contrast.

An ideal approach would combine the advantages of both TCSPC and wide-field microscopy while inheriting as little as possible of their inconvenience. Such an approach has recently been proposed and demonstrated by several groups, using wide-field, time-resolved single-photon counting detectors⁹⁻¹². These detectors allow the precise measurement of the position and arrival time of each detected photon on the image plane. All pixels of the image are therefore populated in parallel, allowing a rapid acquisition of fluorescence decay histograms at each pixel location. However, current detectors have limited global as well as local counting rate capabilities, necessitating image acquisition at very low light level and therefore requiring rather long integration times to obtain a reasonable signal-to-noise ratio (SNR).

Our long term objective is the development of such a detector optimized for single-molecule imaging, which would therefore not need to support very high light levels. Current detectors have rather low detection efficiencies (in the few percents range in the visible spectral window), which are insufficient for efficient single-molecule imaging, due to the small number of photons and limited brightness of single fluorophores. As a first step toward the development of such a wide-field, time-resolved detector adapted to single-molecule imaging, we have designed and built a detector similar to those already commercially available, but incorporating a new position readout scheme that significantly increases the global counting rate. We present here preliminary results of applications of our current detector for fluorescence lifetime imaging microscopy. We conclude with a brief discussion of the general advantages of this type of detector, and the prospects of future detectors currently under development.

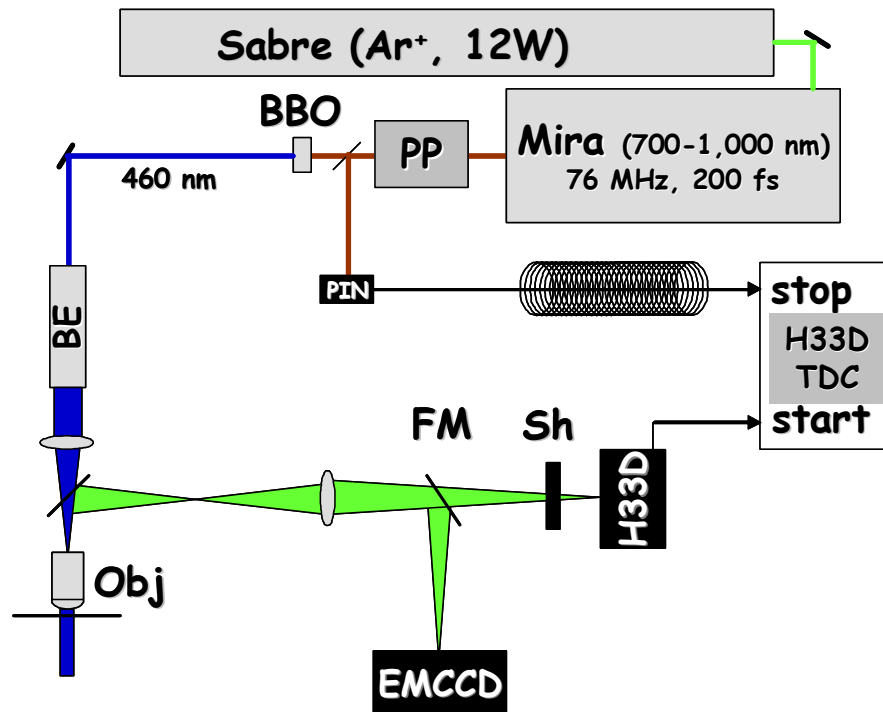


Fig. 1: Wide-field microscopy setup. A pulsed Ti:Sa laser (Mira) pumped by an Ar⁺ ion laser (Sabre) was coupled to a pulse-picker (PP) and frequency-doubled to 460 nm using a BBO crystal. Part of the signal was sent to a fast PIN photodiode and used as a Stop signal for the timing TDC (with a ~ 200 ns delay line). A beam expander (BE) followed by a lens was used to focus the beam at the back of the objective lens (Obj). The signal was collected by a dichroic mirror and filter and imaged onto a wide-field detector (EMCCD or H33D detector depending on the position of the flippable mirror (FM). Some lenses and filters are not represented. Sh: shutter.

2. MATERIAL & METHODS

2.1. Wide-field microscopy setup

The wide-field microscopy setup used in this work is schematically depicted in Fig. 1. Pulsed excitation was provided by the frequency-doubled output of a 76 MHz repetition rate femtosecond Ti:Sa laser (Mira 900, Coherent, Santa Clara, CA) pumped by a 12 W Ar ion laser (Sabre, Coherent). To reduce the repetition rate down to 4.75 MHz, a pulse picker (Model 9200, Coherent) was used. Most experiments were used with an excitation wavelength of 460 nm, obtained after focusing the NIR (920 nm) output of the pulse-picked Ti:Sa onto a BBO crystal (Casix, Mountain Lakes, NJ). The collimated beam was expanded and focused onto the back of a 60x oil immersion microscope objective lens (NA = 1.45, Olympus, Center Valley, PA) with the help of a 458 nm laser long pass dichroic mirror (Z458, Chroma Technology, Rockingham, VT). This configuration results in homogeneous epi-illumination of the sample over an area covering the whole field of view visible by the detector (200 μm diameter in the sample plane). Fluorescence emission was collected by the same objective lens, and imaged with relay lenses onto either an electron multiplying CCD (EMCCD) camera (Cascade 512B, Photometrics, Tucson, AZ) or a wide-field TCSPC detector (H33D detector, described in the next section).

2.2. High-throughput, high temporal and high spatial wide-field single-photon counting (H33D) detector

The H33D detector is based on a previously described custom-designed S20 photocathode+MCP stack+XDL anode assembly sealed in a vacuum tube^{8,10,11}. Its principle is schematized in Fig. 2. It is based on the same principle as other commercially available wide-field, time-resolved photon-counting detectors: a photocathode is followed by a stack of microchannel plates (MCP), which amplify the photo-electrons emitted by the photocathode by several orders of magnitude. The passage of electrons through the MCP stack generates a voltage pulse which is picked up to measure the arrival time of the detected photon with respect to the laser pulse, using standard time-to-digital converter (TDC) electronics (Fig. 1). To match the laser repetition rate, a 200 ns time window was used, resulting in a time resolution of ~50 ps (12 bits). The electron cloud coming out of the back of the MCP is then intercepted by an anode stage and located using dedicated electronics. In our design, the anode consists of two orthogonal meanders of conductive material separated by an insulating layer, forming two cross-delay lines (XDL) with a ~ 0.5mm period. The signal propagation delay of <1 ns/mm and pulse width of < 5 ns are sufficient to achieve <100 μm FWHM resolution for single photon events using high resolution timing electronics. This scheme has been used extensively for many other types of detectors in the past¹³.

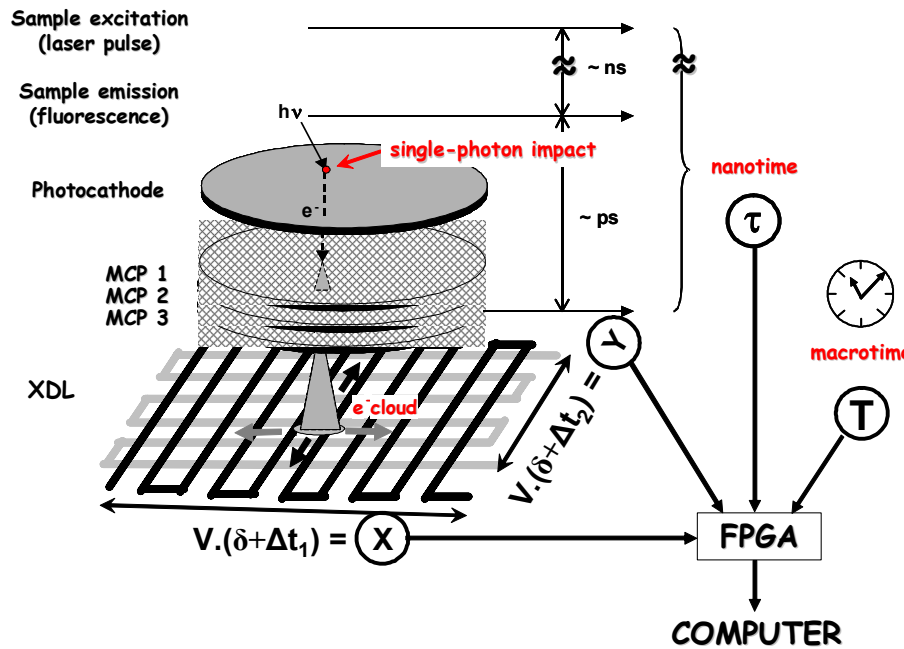


Fig. 2: Principle of the H33D detector. Each photon is converted by the photocathode into a photoelectron amplified $\sim 10^7$ times by the MCP stack. The time interval between the pulse generated at the back of the MCP and the laser pulse (nanotime τ) is measured by a TDC. The electron cloud is collected by a cross-delay line anode (distance to MCP: ~ 6 mm) and a timing electronics module converts the differences in charge arrival time at both ends of the delay lines into position information (X, Y). A laser pulse counter built in the readout electronics provides a 4th coordinate, the macrotime T, which is associated with the 3 other coordinates by a dedicated field-programmable gate array (FPGA), before being sent asynchronously to the computer. δ : fixed time delay. V: velocity factor proportional to the actual anode signal propagation velocity.

2.3. Data analysis

The data acquisition and analysis software was written in LabView (National Instruments, Austin, TX), with some modules written in C (Visual Studio 6.0, Microsoft Corp., Seattle). Raw data (X: 10, Y: 10, τ : 12, T: 24 bits respectively) is continuously saved onto the hard drive in binary format, and processed online to provide different, optional representations: (i) a live intensity image, (ii) an accumulated intensity image, (iii) a live and/or accumulated time-gated image, (iv) intensity time traces corresponding to user-defined regions of interest (ROI) in the live intensity image, (v) accumulated lifetime histograms corresponding to the same ROIs. Lifetime maps are also in principle available but necessitate too much CPU time to be computed online. They were therefore calculated after acquisition.

Lifetime histograms corresponding to ROIs (or the whole image) were exported as ASCII files and analyzed with Origin 7.5 (OriginLab, Northampton, MA) using the non-linear Levenberg-Marquardt (NLLM) algorithm on statistically weighted data and various decay models. The lifetime histogram, fitted function and normalized residuals are represented. Lifetime images were computed using a similar algorithm implemented in LabView. No deconvolution with the instrument response function (IRF) was performed, and time zero was defined as that of the maximum of the lifetime histograms. This simplification may slightly offset the fitted lifetime values, but does not qualitatively affect the results. Fluorescence decay models used in this work are: (i) single-exponential decay, (ii) double-exponential decay, (iii) triple-exponential decay and (iv) stretched exponential decay. For the standard exponential decays, we report the fitted lifetimes τ_i and their respective weights α_i :

$$p_n(t) = A \sum_{i=1}^n \alpha_i e^{-t/\tau_i} + B, \quad \sum_{i=1}^n \alpha_i = 1 \quad (1)$$

(B is the background level). For the stretched exponential decay, we report the fitted lifetime τ , the exponent β and the average lifetime $\langle \tau \rangle = \Gamma(1 + 1/\beta) \cdot \tau$, where Γ is the gamma function¹⁴:

$$p(t) = A e^{-(t/\tau)^\beta} + B \quad (2)$$

Lifetime maps are color-coded and represent the distribution of values of the user-selected parameter resulting from NLLM fit of each pixel lifetime histogram. For instance, for a stretched exponential fit, 6 images can be represented, corresponding respectively to the distribution of A, τ , β , $\langle \tau \rangle$, B and the mean square error. To speed up computation

and increase the number of photons in each pixel histogram, a 8x8 binning of the lifetime images and $N = 256$ time bins were used.

2.4. Samples

Dyes, quantum dots and beads: Erythrosin B (19,826-9, Aldrich Chemical Co, Milwaukee, WI), Rhodamine 6G (RX0090-1, EM Science, Gibbstown, NJ), Ethidium Bromide (E-3565, Molecular Probes, Eugene, OR) and FITC (F-7250, Sigma Chemical Co, St Louis, MO) were used without further purification and after dilution to the appropriate concentration. Samples were prepared by deposition of 10 μ l of solution between two number 1 glass coverslips (25 mm diameter). 511 nm quantum dots (qdots), a gift from Evident Technologies (Troy, NY), were solubilized in water using peptides as previously described¹⁵. Green-yellow fluospheres (100 nm diameter, Excitation/Emission maxima: 505/515 nm, Molecular Probes) were sonicated and centrifugated repeatedly to eliminate aggregates. For ensemble measurements, 10 μ l of solution were prepared as described for the dye samples. For single bead measurements, a diluted sample was spin-cast on a glass coverslip.

Cells: quantum dots emitting at 620 nm and coated with biotinylated peptides were targeted (i) to HeLa cells that stably express a glycosylphosphatidylinositol (GPI)-anchored avidin (GPI-av) as previously described¹⁵ or (ii) to HeLa cells that simultaneously express GPI-av and caveolin 1-EGFP (Cav1-EGFP). A GPI-av/Cav1-EGFP dual expression vector (pFPIG) was produced from the GPI-av encoding pcDNA 3 plasmid¹⁵ and a Cav1-EGFP encoding pEGFP-N1 plasmid (Invitrogen, Carlsbad, CA) which was a gift of Dr. H. P. Moore (Dept Molecular & Cell Biology, UC Berkeley, CA). HeLa cells were then transfected with linearized pFPIG using Effectene reagent (Qiagen, Valencia, CA) and stable clones were selected with 0.75 mg/ml G418 (Invitrogen). For imaging, HeLa cells were grown in DMEM media supplemented with 5 % fetal calf serum (FCS) on fibronectin coated temperature-regulated wells (SmartSlide 100, Wavergen, Fremont, CA). Cells were kept at 37°C through all labeling steps and during imaging. 3 to 4 hours prior to labeling with qdots, the cells were starved in DMEM media to free the GPI-av proteins from biotin present in the FCS supplement and avoid competition with the biotinylated qdots. Cells were pre-incubated in a HBSS + 1% BSA buffer for 10 min before the addition of 10 nM qdots and further incubation for 20 min. Cells were then rinsed with HBSS or

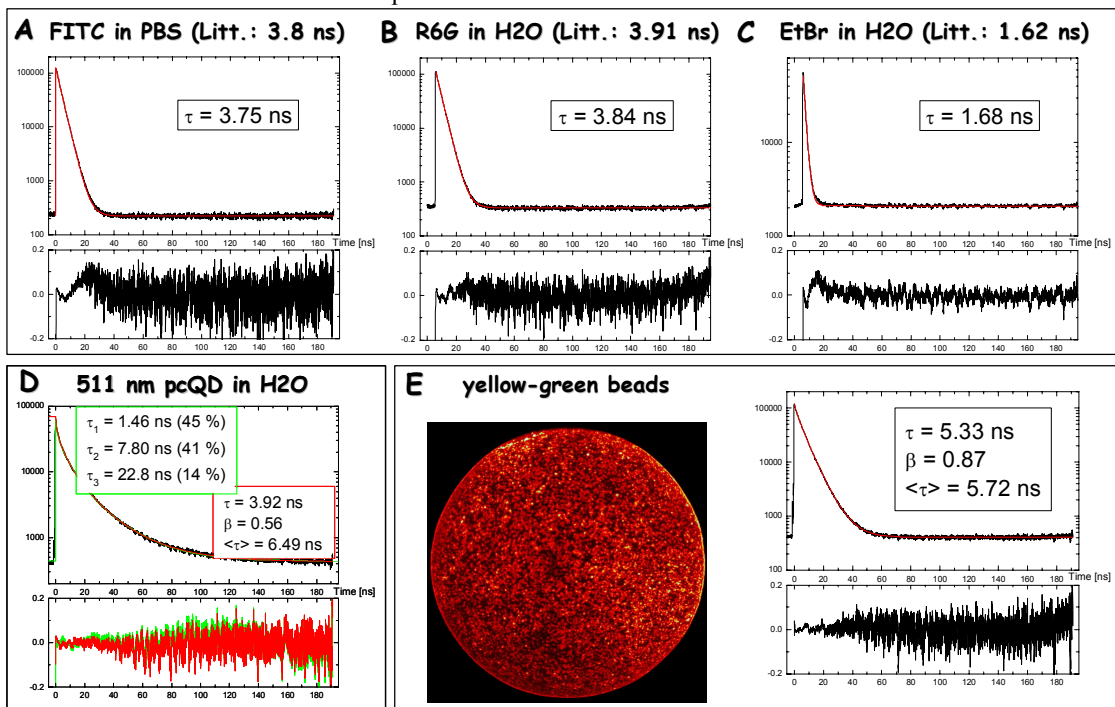


Fig. 3: Ensemble lifetime measurements. A-D: solution samples. E: spin-cast bead sample. The lifetime decays (black histogram, top panel) correspond to all photons in the image area ($\sim 200 \mu$ m diameter in the sample plane). The fitted decay (red curve), fitted parameters and normalized residuals (lower panel) are also represented. A-C: single-exponential fit. D: triple-exponential fit (green) and stretched exponential fit (red). E: stretched exponential fit. In E, the corresponding image of spin-cast beads is also shown to show that individual beads can clearly be identified.

FCS-free DMEM at 37°C and imaged. In other experiments, non-biotinylated peptide-coated qdots were incubated overnight with HeLa cells, resulting in non-specific endocytosis. Cells were then rinsed with DMEM medium and imaged at 37°C.

3. RESULTS

3.1. Instrument response function

The instrument response function (IRF) of the whole acquisition setup was measured using a solution of Erythrosin B in water and the different filters used in the experiments. Erythrosin B has a ~80 ps fluorescence lifetime, and therefore should contribute minimally to the width of the IRF, which was found to have a typical full-width-at-half-maximum (FWHM) of ~250 ps. The IRF can approximately be fitted by a single exponential decay with time constant 150 ps.

3.2. Ensemble lifetime measurements

A good test of the lifetime measurement capabilities of a system consist in measuring the fluorescence lifetime of well-known samples. Fig. 3A-C shows 3 standard dye samples measured as described in Materials & Methods: FITC, Rhodamine 6G (R6G) and Ethidium Bromide. The fitted lifetimes (without deconvolution by the IRF) are in excellent agreement with the published values^{9,16}. The qdot sample (Fig. 3D) is best fitted with a triple exponential decay and exhibits two long lifetime components. It is equally well fitted with the much simpler stretched exponential model. Interestingly, the spin-cast fluorescent bead sample (Fig. 3E) also requires more than one decay constant to be fitted properly. This lifetime heterogeneity is similarly observed in an ensemble measurement of beads in solution, and has previously been reported for FITC-doped silica beads¹⁷. Multiple mechanisms have been proposed with limited success to account for this phenomenon. Preliminary measurements of individual bead lifetime decays fitted with a single-exponential decay seem to indicate that different beads are characterized by different fluorescence lifetimes, pointing to a static origin of the observed heterogeneity. Future work will clarify this issue.

3.3. Live cell imaging

As a demonstration of the fluorescence lifetime imaging capabilities of the H33D detector, we thought of using a sample exhibiting two markedly different lifetimes. We therefore chose a cell line stably expressing two chimeric proteins: a GFP-caveolin fusion, expected to be expressed and translocated to caveolae (thus on the cell surface), and a GPI-anchor/Avidin, expected to be translocated to the external leaflet of the cell membrane^{15,18}, and therefore detectable by externally provided biotinylated qdots. GFP is expected to have a lifetime of ~ 2.5 ns and emit in the green region of the spectrum, whereas 620 nm qdots have long lifetimes (> ~10 ns) and emit in the red, which should make both easily distinguishable without spectral separation. Whereas the cells behaved as expected, it turned out to be difficult to obtain a properly balanced level of expression of both proteins, or labeling level of the GPI-anchor/Avidin construct that resulted in a contrasted lifetime map. We therefore resorted to a simpler approach consisting in using non-biotinylated qdots and incubating them overnight, in order to allow massive endocytosis and endosomal localization of qdots. As illustrated in Fig. 4 in one extreme example, even though the two signals could easily be observed and their location determined precisely when observed in their individual spectral channel (530 ± 15 nm for GFP, 615 ± 22 nm for the 620 nm emitting qdots), attempting to observe them both simultaneously using a non discriminating filter (long pass 500 LP) resulted in an image dominated by the qdot signal (the opposite being true in other cases). This imbalance is fatal for lifetime separation as is well known from practitioners of multi-exponential fitting. The whole image fluorescence decay histograms shown in Fig. 4 illustrate this point further, showing that the contribution of the GFP signal minimally affects the global fluorescence decay. This small effect is even less visible when observed at the single pixel level (or even with 8x8 binning), and results in lifetime maps with little or no contrast, whichever decay model is used (data not shown).

Although not fully conclusive as far as demonstrating the power of lifetime imaging (which is on the other hand well-established in the literature), this series of observations nevertheless demonstrates the capability of our detector to acquire high-resolution images of live cells in different spectral channels, at rather large count rates (up to several 100 kHz) and with high temporal resolution. Future work on better suited samples will fully exploit this potential.

4. DISCUSSION

4.1. Theoretical comparison between scanning and wide-field FLIM

For a comparison of the respective merits of both approaches, which have been debated in the literature^{2,9}, wide-field (WF) and point detectors can be characterized by their maximum local (r_w , r_s) and global (R_w , R_s) count rates. If p^2 is

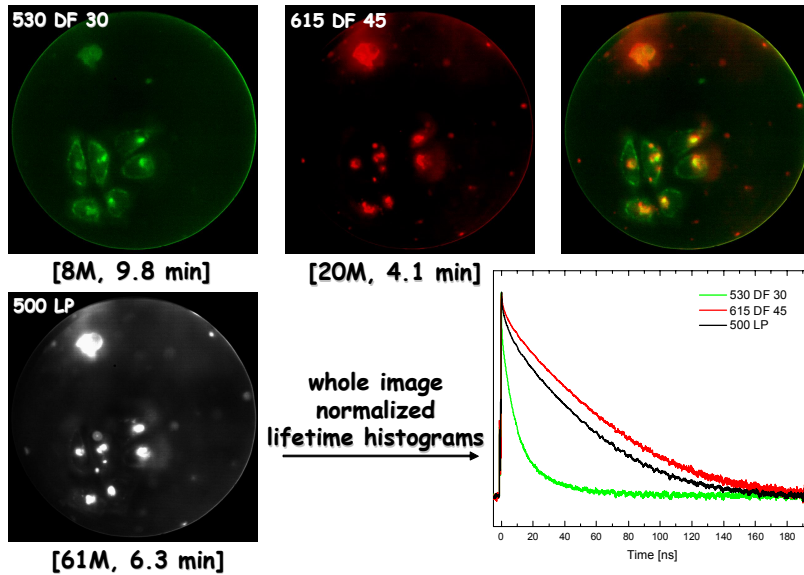


Fig. 4: HeLa cell imaging. Top panel, from left to right: caveolin-GFP signal (Filter: 530 D 30), qdot signal (615 DF 45) and overlay. Bottom panel: both signal are detected simultaneously using a long pass filter (500 LP). The dominance of the qdot signal is readily visible in the intensity image, but shows up similarly in the fluorescence decay curve of the whole image (black curve), which is barely different from the qdot only channel (red curve). This situation is best quantified by the number of photons detected for each type of fluorophores (numbers in millions of photons below each image) versus the acquisition time (in minutes). The qdot signal is evidently much more intense than the GFP signal, thus making it very difficult to separate both in a lifetime image map (data not shown).

the number of pixels of the WF detector (as well as in the raster-scanned image), generally, $R_w < p^2 r_w$ (i.e. not all pixels can simultaneously collect a count rate of r_w , as soon as p is large enough, since typically $R_w = 100-1000 r_w$). On the other hand, the maximum global count rate in the point detection scheme is easily calculated as $R_s = (p^2 r_s dT)/T$, where $T = p^2 dT$ is the total scan duration, dT being the integration time per pixel. Hence $R_s = r_s$ for the point detection scheme. In conclusion, as soon as $R_w > r_s$, i.e. the maximum global count rate of the WF detector is larger than the maximum local count rate of the point detector, the former allows a faster image acquisition. The gain in acquisition time roughly scales as R_w/r_s . Of course this analysis assumes that the detected signal on both types of detectors is similar, such that the resulting image has the same contrast. If one detector has a lower quantum efficiency (QE), this can be obtained by boosting the excitation laser power (up to a certain extent, in order to prevent bleaching or saturation). The current H33D detector has a maximum local count rate of ~ 10 kHz (limited by the MCP stack) and a maximum global count rate of ~ 500 kHz (although this depends on the TDC time window, and neglects the onset of saturation effects at around half this value, data not shown). With typical count rates of point detectors used in FLIM usually limited to a few 100 kHz^2 , this type of detector is already in good position to compete with scanning FLIM approaches.

However, as noted in the introduction, wide-field detection does not remove out-of-focus emission, which tremendously reduces image contrast, unless multiple images are acquired using structure illumination, or using 3-dimensional deconvolution. It seems therefore that unless very little background autofluorescence is generated in the sample, scanning-confocal FLIM might be preferable. A potential application of WF detectors such as the H33D could thus be in total internal reflection (TIR) FLIM imaging, where a thin surface layer of ~ 100 nm only is excited in the sample. Future work will explore this potentiality.

4.2. Future capabilities of H33D detectors

As we have argued previously, the current H33D detector is a proof-of-concept prototype, demonstrating the advantages of a faster anode readout system (XDL) over older resistive anode schemes. Several design limitations can be identified: (i) the S20 anode has a limited QE in the visible part of the spectrum of practical interest for life science, and is insufficient for single-molecule spectroscopy and imaging; (ii) the maximum local count rate is too low to permit imaging at very high frame rates; (iii) the maximum global count rate is limited. Fortunately, all these limitations have solutions.

On one hand, new developments in photocathode technology (fast GaAs, fast GaAsP, etc) should allow QE of up to 20-40% in the visible to be obtained. This is not so far from the best current point detectors, or even from CCDs, and would definitely allow single-molecule observation and very high frame rate imaging. The second limitation has a well-identified origin: the maximum local count rate is directly linked to saturation of MCPs and decrease of their gain at high count rates. Two possible solutions exist: either reduce the gain of the MCPs (which requires anodes capable of acquiring the position of each event with smaller electron clouds), or use MCPs with lower resistance. Cross-strip (XS)

anodes developed for astronomy detectors¹⁹ have the kind of performance that would preserve the resolution of the current H33D detector but at much lower gain levels, allowing local count rates of up to 100 kHz to be sustained. The current global count rate limitation (point iii) is due to the dead-time of the timing and readout electronics. New XDL readout electronics developed at UCB will allow global count rates up to 2 MHz, while cross-strip anode electronics and fast TDC modules should achieve ~5 MHz global count rates. We are actively exploring all these avenues and anticipate that future H33D detector generations will have applications beyond single-molecule spectroscopy and imaging that we originally had in mind.

ACKNOWLEDGMENTS

We thank Gopal Iyer for providing us with the green pc-qdot sample used in this work.

This work was supported by NIH Grant 5 R21 RR017474 and in part by NIH Grant 5 R01 EB000312.

REFERENCES

1. Suhling, K.; French, P. M. W.; Phillips, D. "Time-resolved fluorescence microscopy". *Photochem. Photobiol. Sci.* **2005**, *4*, 13.
2. Becker, W. *Advanced time-correlated single photon counting techniques*; Springer: Berlin, 2005.
3. van Munster, E. B.; Gadella, T. W. J. "Fluorescence Lifetime Imaging (FLIM)". *Adv. Biochem. Engin. Biotechnol.* **2005**, *95*, 143.
4. Suhling, K. Fluorescence lifetime imaging. In *Cell Imaging*; Stephens, D., Ed.; Scion Publishing Ltd: Bloxham, 2006.
5. Lakowicz, J. R. *Principles of Fluorescence Spectroscopy*, 2 ed.; Plenum: New York, 1999.
6. Watanabe, M.; Koishi, M.; Fujiwara, M.; Takeshita, T.; Cieslik, W. "Development of a new fluorescence decay measurement system using two-dimensional single-photon counting". *Journal of Photochemistry and Photobiology A: Chemistry* **1994**, *80*, 429.
7. *Handbook of biological confocal microscopy*; Pawley, J. B., Ed.; Plenum Press: New York, 1995.
8. Michalet, X.; Siegmund, O. H. W.; Vallerger, J. V.; Jelinsky, P.; Millaud, J. E.; Weiss, S. "Detectors for single-molecule fluorescence imaging and spectroscopy". *J. Mod. Opt.* **2006**, *in press*.
9. Emiliani, V.; Sanvitto, D.; Tramier, M.; Piolot, T.; Petrasek, Z.; Kemnitz, K.; Durieux, C.; Coppey-Moisan, M. "Low-intensity two-dimensional imaging of fluorescence lifetimes in live cells". *Appl. Phys. Lett.* **2003**, *83*, 2471.
10. Michalet, X.; Siegmund, O. H. W.; Vallerger, J. V.; Jelinsky, P. N.; Millaud, J. E.; Weiss, S. "Photon-Counting H33D Detector for Biological Fluorescence Imaging". *Nucl. Instrum. & Meth. A* **2006**, *567*, 133.
11. Michalet, X.; Siegmund, O. H. W.; Vallerger, J. V.; Jelinsky, P.; Millaud, J. E.; Weiss, S. "A space- and time-resolved single-photon counting detector for fluorescence microscopy and spectroscopy". *SPIE Proc.* **2006**, *6092*, 60920M.
12. Ecker, H.-J.; Petrášek, Z.; Kemnitz, K. "Application of novel low-intensity non-scanning fluorescence lifetime imaging microscopy for monitoring excited state dynamics in individual chloroplasts and living cells of photosynthetic organisms". *SPIE Proc.* **2006**, *6372*, *in press*.
13. Siegmund, O. H. W.; Gummin, M. A.; Stock, J.; Marsh, D.; Raffanti, R.; Sasseen, T.; Tom, J.; Welsh, B.; Gaines, G.; Jelinsky, P.; Hull, J. "Delay Line Detectors for the UVCS and SUMER Instruments on the SOHO Satellite". *Proc. SPIE* **1994**, *2280*, 89.
14. Lee, K. C. B.; Siegel, J.; Webb, S. E. D.; Leveque-Fort, S.; Cole, M. J.; Jones, R.; Dowling, K.; Lever, M. J.; French, P. M. W. "Application of the stretched exponential function to fluorescence lifetime imaging". *Biophys. J.* **2001**, *81*, 1265.
15. Pinaud, F.; King, D.; Moore, H.-P.; Weiss, S. "Bioactivation and Cell Targeting of Semiconductor CdSe/ZnS Nanocrystals with Phytochelatin-Related Peptides". *J. Am. Chem. Soc.* **2004**, *126*, 6115.
16. Haugland, R. P. *Handbook of fluorescent probes and research products*, 9 ed.; Molecular Probes: Eugene, 2002.
17. Imhof, A.; Megens, M.; Engelberts, J. J.; de Lang, D. T. N.; Sprik, R.; Vos, W. L. "Spectroscopy of Fluorescein (FITC) Dyed Colloidal Silica Spheres". *J. Phys. Chem. B* **1999**, *103*, 1408.
18. Michalet, X.; Pinaud, F. F.; Bentolila, L. A.; Tsay, J. M.; Doose, S.; Li, J. J.; Sundaresan, G.; Wu, A. M.; Gambhir, S. S.; Weiss, S. "Quantum Dots for Live Cells, in Vivo Imaging, and Diagnostics". *Science* **2005**, *307*, 538.
19. Tremsin, A. S.; Siegmund, O. H. W.; Vallerger, J. V.; Hull, J. S.; Abiad, R. "Cross-strip readouts for photon counting detectors with high spatial and temporal resolution". *IEEE Trans. Nucl. Sci.* **2004**, *51*, 1707.